COMPUTER METHODS IN MATERIALS SCIENCE

2024, vol. 24, no. 2, 5–25
https://doi.org/10.7494/cmms.2024.2.0834

Modeling the thermo-mechanical response and phase changes in metallic additive manufacturing (MAM) processes using a dissipative phase-field model

Roya Darabi*, Erfan Azinpour, Ana Reis, Jose Cesar de Sa

Faculty of Engineering of University of Porto (FEUP), FEUP campus, Rua Dr. Roberto Frias, 400, Porto, 4200-465, Portugal.

Abstract

Additive manufacturing (AM) has emerged as a highly promising manufacturing technique, offering unprecedented possibilities for creating complex geometries and functional structures. However, harnessing the full potential of AM requires the development of a robust computational framework capable of capturing the intricate multi-scale and multi-physics nature of the process. The constitutive and structural responses encountered in AM are particularly challenging to reproduce due to the complex behavior of the material involved. This research aims to address these challenges by presenting a comprehensive computational approach that incorporates a material model capable of accurately representing the behavior of different phases occurring during AM. To achieve this, the finite element method, using the Lagrangian framework in the implicit time scheme, is employed through the widely adopted ABAQUS software. Computational implementation is facilitated using the FORTRAN programming language. By employing weakly coupled thermal and mechanical constitutive equations, the framework enables the analysis of thermal stresses, strains, and displacements during realistic solidification processes, which inherently involve highly nonlinear constitutive relations. Through a series of numerical examples, the capabilities of the proposed model are demonstrated across various computational scales, particularly during the rapid melting and solidification phases. These simulations reveal the formation of residual stresses, which can lead to part distortion and have detrimental effects on the mechanical properties of the manufactured components. This research contributes to the advancement of additive manufacturing by providing a reliable computational tool that integrates the complex interplay between thermal and mechanical phenomena. The developed framework enhances our understanding of the AM process, offering valuable insights into the factors influencing the structural integrity and performance of additively manufactured parts.

Keywords: metallic additive manufacturing, direct energy deposition, finite element method, ABAQUS, phase transformations, residual stress

1. Introduction

Additive manufacturing (AM) is a manufacturing process that involves the sequential addition of material to fabricate a part, offering advantages over subtractive manufacturing or molding. It enables the production of low-volume, customized products with complex geometries in a relatively short time and at a reasonable cost. AM is often referred to as a near-net-shaping technology, as the part is directly constructed based on a computer-aided design (CAD) model. To facilitate the AM process, the CAD model is converted into

* Corresponding author: rdarabi@inegi.up.pt
ORCID ID's: 0000-0002-0807-0156 (R. Darabi), 0000-0003-1018-7123 (E. Azinpour), 0000-0003-0256-1488 (A. Reis), 0000-0002-1257-1754 (J. Cesar de Sa)

a standard triangulation language (STL) format, which is widely compatible with different AM machines. The STL file represents the geometry of the CAD model through a simple segmentation. This digital file is then sliced into thin cross-sectional layers, allowing the part to be constructed layer by layer according to the chosen AM process parameters. ASTM standard F2792 (ASTM International, 2013) categorizes AM into two main types: powder bed fusion (PBF) (Chua et al., 2024; Horn et al., 2024; Warner et al., 2024) and directed energy deposition (DED) (Thompson et al., 2015; Zhou et al., 2024). In DED machines, a nozzle mounted on a multi-axis arm deposits material in the form of powder onto the designated surface, where it solidifies. A laser beam serves as the heat source, partially melting the metallic powder particles according to the CAD model. The material then solidifies after a cooling period. This layering and solidification process is repeated until the final geometry of the workpiece is achieved, with local re-melting and re-solidification occurring as the laser passes over prior layers. Consequently, complex parts can be manufactured by melting metallic powder layer by layer, enabling lightweight construction and the incorporation of intricate internal structures. This technology finds applications in industries such as aerospace and automotive. Despite these merits, there is still a significant knowledge gap regarding the influence of process parameters on the properties of final parts, particularly when one is aiming for mass production. Understanding these effects is crucial for consistent and reliable manufacturing in large-scale production scenarios. The application of the finite element method (FEM) to solve heat transfer problems was proposed by Zienkiewicz in 1979 (Zienkiewicz et al., 2013) and Hughes (1987). Interested readers are encouraged to refer to these excellent resources for further exploration. In the context of additive manufacturing, the utilization of FEM for simulating selective laser sintering (SLS) was first introduced by Marcus et al. (1992). Since then, numerous studies have been conducted in the field of modeling thermomechanical processes in directed energy deposition (DED) using various commercial software or in-house codes, as evidenced by the literature (Crespo & Vilar, 2010; Heigel et al., 2015; Labudovic et al., 2003; Stender et al., 2018; Wang J.-h. et al., 2019; Wang Q. et al., 2017). Thermomechanical models play a crucial role in predicting residual stresses, geometries, and the impact of trajectory strategies on the final part. In the directed energy deposition process, a short-term interaction occurs between the powder particles and the high-energy laser beam before the powder particles enter the melt pool. This interaction results in laser energy attenuation (Wang J.-h. et al., 2019) and non-linear temperature increases in the powder particles (Tan et al., 2020). Consequently, the model must accurately consider the laser-powder particle interaction during melting, powder consolidation, and solid-liquid phase changes. However, this poses significant computational challenges due to the complexity of the model and the multi-scale nature of the process (Darabi et al., 2023). Within the computational domain surrounding the laser source, three distinct material phases exist: powder, molten, and solidified. These phases exhibit significantly different mass densities, leading to process-induced eigenstrains during phase changes (Noll et al., 2020). Various approaches have been proposed to model these phase changes. For instance, the model by Hodge et al. (2014) enhances the Stefan–Neumann equation, while Kollmannsberger et al. (2019) employs a mathematical phase change function. Another effort by Roy et al. (2018) applies the thermodynamic phase field model for solidification, allowing the investigation of phase-dependent laser absorptivity in selective laser melting (SLM). In another attempt, the same group (Darabi et al., 2022) modeled the directed energy deposition process, including the phase change phenomena with an approximated function in the mushy zone, transitioning from powder to molten and then to solidified phases in the thermal sequence of the problem, without considering the effect of mechanical response on temperature behavior. Furthermore, they extended their study to a fully coupled thermo-mechanical phase field model (Darabi et al., 2023), incorporating the Allen–Cahn formulation to consider the effect of phase changes on the mechanical response for powder bed fusion. However, in our view, there is currently a deficiency in integrated frameworks that comprehensively consider both the mechanical material model and phase change in a physically motivated approach. This research introduces a novel approach and finite element formulation for modeling the melting, consolidation, and re-solidification processes in directed energy deposition (DED). To investigate solidification phenomena and the crystallization of a pure substance from its molten state, a class of phase field models based on the entropy function proposed by Penrose & Fife (1990) is developed. This model, ensuring continuous positive entropy production locally, incorporates an additional nonlinear function of the phase field to ensure thermodynamic consistency as utilized in the papers by Wang S.-L. et al. (1993) and Gonzalez-Ferreiro et al. (2014). Initially, the equivalence of the phase function with a thermodynamically consistent phase field approach is validated. Subsequently, a new material state variable, termed consolidation, is introduced to track the phase change

between the powder and molten material. The introduction of the consolidation state variable enables the prediction of porosity in the final part and facilitates the incorporation of consolidation effects on material properties, energy absorption function, and geometric evolution. A Lagrangian finite element formulation that solves the governing heat equations in a fixed reference configuration is derived. This formulation naturally accounts for the changing geometry as the powder phase melts, eliminating the need to update the simulation domain. Several assumptions are made: (i) no flow consideration (velocity field is zero), (ii) stress-free configurations during evolution, (iii) homogeneity, isotropy, and incompressibility of the domain regarding the phase, and (iv) the absence of viscous effects in the energy equation. A transient, fully implicit integration algorithm is employed, enabling relatively large time steps due to its unconditionally stable nature. The finite element model is implemented in ABAQUS, utilizing provided user subroutines along with a graphical interface module. Using stored field variables that represent the material point phase configuration throughout the simulation, a sequential mechanical analysis is conducted to account for thermal loading. The constitutive equilibrium mechanical equations, considering strain hardening and annealing effects, are incorporated, and element deactivation techniques are applied to the powder state material due to its negligible stiffness. Firstly, the proposed model is validated by comparing it with simulation results from the single-track scanning process, utilizing experimentally measured melt pool dimensions from previous studies by the same authors. Subsequently, a thin-walled structure undergoing multiple re-melting cycles is simulated, obtaining the stress field through sequentially coupled thermo-mechanical analysis. Finally, the influence of different stress components on the stability of the thin-walled part is evaluated. Figure 1 schematically illustrates the approach employed and the computational stages involved in this research. This article is structured as follows: In section 1, detailed thermodynamic field equations modified to accommodate the positive entropy model for phase change in additive manufacturing processes are presented. In section 2, the implementation of the finite element method (FEM) code for solving transient heat equations using the ABAQUS environment is described. Section 3 focuses on the constitutive mechanical formulation, which is incorporated into the FEM formulation to model induced residual stresses and deformations. To provide a comprehensive understanding of the developed user codes, numerical calculations conducted at the material point level to demonstrate the proof of concept are presented in section 4. Additionally, representative three-dimensional boundary value problems to showcase the application of the developed codes are presented. Finally, in section 5, the key findings and conclusions drawn from this study are summarized.

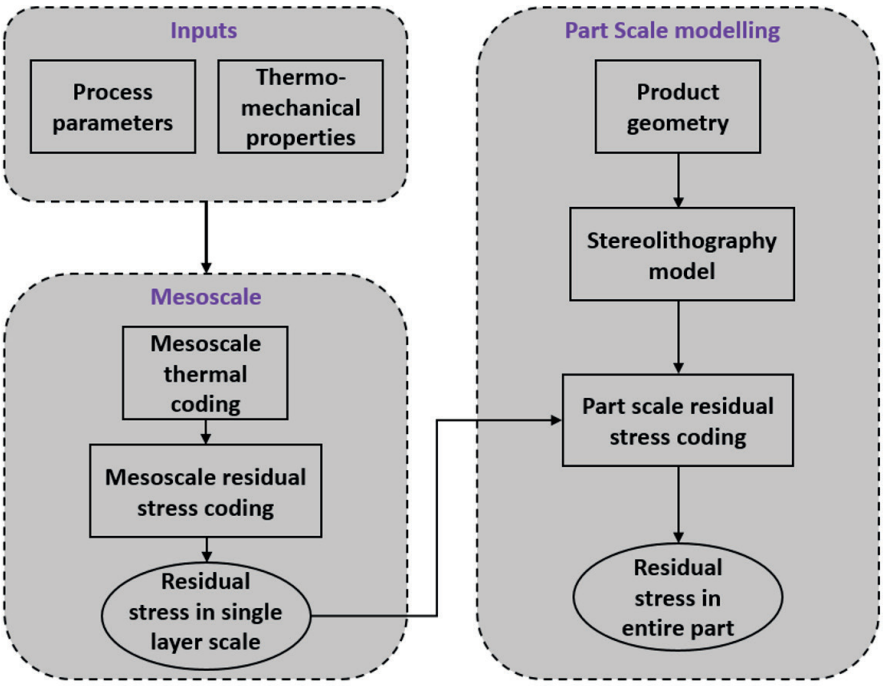

Fig. 1. Schematic representation demonstrating the utilization of predicted results from the mesoscale model to calculate residual stresses and strains at the part scale

2. Governing local equations in thermomechanics

This section presents the local governing equations in thermomechanics, emphasizing a general thermomechanical formulation with phase-change phenomena, constitutive relations, energy balance, and specific thermoelastoplastic models. These foundational equations and relations guide the study of thermomechanical behavior in materials, accounting for phase changes, temperature effects, and elasto-plastic deformation.

2.1. Constitutive thermal equations

Referring to Wang S.-L. et al. (1993), for every subvolume v of V, let ψ denote its total energy. Since energy is an extensive property, it can be expressed as:

$$\psi = \int_{\Omega} e\, dv \tag{1}$$

where e represents the energy density. According to the first law of thermodynamics, the change in energy within a subset Ω is determined by the thermal power entering through its boundary Γ. This can be expressed as:

$$\dot{\psi} + \int_{\Gamma} \mathbf{q}\cdot\mathbf{n}\, da = 0 \tag{2}$$

Here, $\dot{\psi}$ represents the rate of change of energy within Ω over time, and $\mathbf{q}\cdot\mathbf{n}$ represents the heat flux normal to the surface Γ. This equation ensures the conservation of energy within Ω, where the left-hand side represents the rate of energy change and the right-hand side represents the net heat flux entering Ω through its boundary Γ. Using the divergence theorem, the surface integral can be converted into a volume integral:

$$\dot{\psi} + \int_{\Omega} \nabla\cdot\mathbf{q}\, dv = 0 \tag{3}$$

where $\nabla\cdot\mathbf{q}$ represents the divergence of the heat flux vector $\mathbf{q}$. Since this equation holds for any subset Ω, the integrands can be equated to obtain the differential expression:

$$\dot{e} + \nabla\cdot\mathbf{q} = 0 \tag{4}$$

The entropy of any subvolume Ω of V is assumed to be represented by the functional:

$$S = \int_{\Omega}\left[\eta - \frac{1}{2}\epsilon^2\,(\nabla\phi)^2\right] dv \tag{5}$$

where S represents the entropy functional for the subvolume Ω, $\eta(e, \phi)$ is an entropy density extending classical thermodynamics, applying to a uniform system of internal energy density e, phase field ϕ, and ϵ is a constant (Wang S.-L. et al., 1993). The second term of the integral is based on the Cahn–Hilliard (Novick-Cohen, 2008) or Landau–Ginzburg (Duxbury, 2011) gradient energy term in the free energy term. According to Gonzalez-Ferreiro et al. (2014), the differentiation of Equation (5) with respect to time can be expressed as:

$$\dot{S} = \int_{\Omega}\left\{\left(\frac{\partial\eta}{\partial e}\right)_{\phi}\dot{e} + \left[\left(\frac{\partial\eta}{\partial\phi}\right)_{e} + \epsilon^2\,\nabla^2\phi\right]\dot{\phi} - \epsilon^2\,\nabla\cdot(\dot{\phi}\nabla\phi)\right\} dv \tag{6}$$

Here, $\dot{e}$ is replaced from Equation (4), and the Gauss theorem is utilized for integration by parts. The new form of Equation (6) yields:

$$\begin{aligned}\dot{S} = &\int_{\Omega}\left\{\mathbf{q}\cdot\nabla\left(\frac{\partial\eta}{\partial e}\right)_{\phi} + \left[\left(\frac{\partial\eta}{\partial\phi}\right)_{e} + \epsilon^2\,\nabla^2\phi\right]\dot{\phi}\right\} dv \\ &-\int_{\Gamma}\left[\left(\frac{\partial s}{\partial e}\right)_{\phi}\mathbf{q} + \epsilon^2\,\dot{\phi}\nabla\phi\right]\cdot\mathbf{n}\, da\end{aligned} \tag{7}$$

According to the second law of thermodynamics, entropy production should be positive in any subvolume Ω of V. The entropy production can be calculated by subtracting from $\dot{S}$ the entropy flux through Γ, resulting in the following relationship:

$$\dot{S} + \int_{\Gamma}\left[\left(\frac{\mathbf{q}}{T}\right)\cdot\mathbf{n} + \epsilon^2\,\dot{\phi}\nabla\phi\cdot\mathbf{n}\right] d\Gamma \geq 0 \tag{8}$$

In this case, T represents temperature, and $\mathbf{q}/T$ represents the entropy flux associated with heat flow. The term $\epsilon^2\nabla^2\phi$ corresponds to an entropy flux related to the variation in the phase field at the boundary of the subvolume Ω. By substituting Equation (7) into Equation (8), it is obtained:

$$\int_{\Omega}\left\{\mathbf{q}\cdot\nabla\left(\frac{1}{T}\right) + \left[\left(\frac{\partial\eta}{\partial\phi}\right)_{e} + \epsilon^2\,\nabla^2\phi\right]\dot{\phi}\right\} d\Omega \geq 0 \tag{9}$$

To obtain the governing energy balance equation and the entropy evolution,the first law of thermodynamics, which prescribes the conservation of internal energy, is started from as:

$$de = Tds + \left(\frac{\partial e}{\partial\phi}\right)_{\eta} d\phi \tag{10}$$

where $(\partial\eta/\partial e)_{\phi} = 1/T$ and T is temperature. Additionally, to ensure a positive local entropy production, Equations (11) and (12) are proposed:

$$\mathbf{q} = M_T\nabla\left(\frac{1}{T}\right) \tag{11}$$

$$\dot{\phi} = \frac{1}{\tau}\left\{-\frac{1}{T}\left(\frac{\partial e}{\partial\phi}\right)_{\eta} + \epsilon^2\,\Delta\phi\right\} \tag{12}$$

where M_T and τ are both positive parameters. With the help of the Clausius–Duhem inequality (Alart et al., 2006) (Equation (9)), the definition of specific Helmholtz free energy ψ is:

$$\psi = e - T\eta \tag{13}$$

By combining the differential of the aforementioned equation with Equation (10), the following expression is obtained:

$$\left(\frac{\partial e}{\partial \phi}\right)_{\eta} = \left(\frac{\partial \psi}{\partial \phi}\right)_{T} \tag{14}$$

$$\left(\frac{\partial \psi}{\partial T}\right)_{\phi} = -\frac{e}{T^2} \tag{15}$$

The expression for ψ in Equation (13) can be written as:

$$\psi = T\left(\int_{T}^{T_m} \frac{e(\phi,\zeta)}{\zeta^2} d\zeta + G(\phi)\right) \tag{16}$$

where $G(\phi)$ is a function of ϕ that is yet to be determined, and T_m denotes the temperature at which melting occurs. Consequently, $G(\phi)$ is opted to be a symmetric 'double well' potential, characterized by minima at zero and unity. The chosen functional form is:

$$G(\phi) = \phi^2(1-\phi)^2 \tag{17}$$

It is assumed here that the internal energy density takes the form given by Roy et al. (2018):

$$e = c_s(\phi)T + p(\phi)\left[L + (c_l - c_s(\phi))(T - T_m)\right] \tag{18}$$

where c_l and $c_s(\phi)$ are the volumetric heat capacities of the liquid and solid phases, respectively. L is the latent heat of phase change between fusion and melting. T_m is the melting temperature, and ϕ represents the consolidation factor, which will be elaborated further. Herein, $c_s(\psi)$ denotes the effective heat capacity c_d, incorporating the initial porosity effect ϵ_0:

$$c_s(\psi) = (1 - \epsilon_0 (1-\phi))c_d \tag{19}$$

According to Wang S.-L. et al. (1993), the function $p(\phi)$ is polynomial:

$$p(\phi) = \phi^3(10 - 15\phi + 6\phi^2) \tag{20}$$

These considerations lead to the derivation of the classical heat equation in the bulk solid and liquid:

$$\frac{de}{dT}\frac{dT}{dt} - k(\phi)\nabla^2 T + Q = 0 \tag{21}$$

where $M_T = kT^2$ (from Equation (11)), $k(\phi)$ being the thermal conductivity, Q the external heat supply per unit volume, and $k(\phi)$ incorporating consolidation dependency. In detail, $k(\psi)$ represents the thermal conductivity, which is a combination of the powder phase (k_p) and the fully dense material phase (k_d):

$$k(\psi) = (1-\psi)k_p + \psi k_d \tag{22}$$

Additive manufacturing involves directing an energy source to melt powder layers that subsequently condense and solidify on the substrate or preceding layers. To distinguish between phases during the manufacturing process, two state variables are utilized: ψ and ϕ. Here, $0 \le \psi, \phi \le 1$, where ψ is the consolidation parameter: ψ = 1 denotes full density, while ψ = 0 indicates a powdered state. ϕ represents the phase parameter, with ϕ = 0 indicating a fully solid region and ϕ = 1 representing the molten phase. The condition $\psi(x, t + \Delta t) \ge \psi(x, t)$ ensures the irreversibility of the phase change from powder to molten phase, where $\psi(x, t + \Delta t)$ represents the phase field variable for consolidation in the current time increment, and $\psi(x, t)$ denotes its value in the previous increment. Figure 2 illustrates the combination of these phases in the metal additive manufacturing process. The subsequent section elaborates on the dedicated state variables in detail.

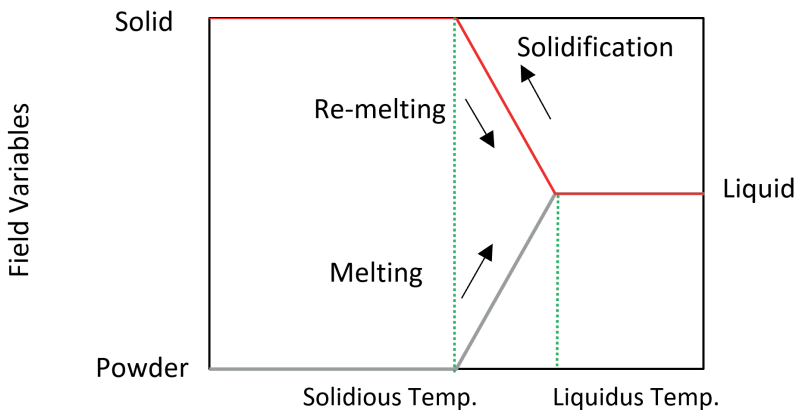

Fig. 2. Diagram illustrating phase changes between powder, liquid, and solid states

From Roy et al. (2018), Equation (12) gives:

$$\dot{\phi} = \frac{1}{\tau} p'(\phi)\left[\left(\frac{L}{T_m} - c_l + c_s(\phi)\right)\left(1 - \frac{T_m}{T}\right) + (c_l - c_s(\phi))\ln\left(\frac{T}{T_m}\right)\right] - \frac{1}{2} a\phi(1 - 3\phi + 2\phi^2) + \epsilon^2 \Delta\phi \quad (23)$$

where τ, a, and ϵ are parameters related to interface thickness δ, interface energy σ, and interface mobility μ:

$$\tau = \frac{6\sqrt{2}\delta L}{\mu T_m^2} \quad (24)$$

$$a = \frac{\sqrt{2}\delta T_m}{12\sigma} \quad (25)$$

$$\epsilon^2 = \frac{\delta^2}{a} \quad (26)$$

The phase-field method inherently uses a diffuse interface with ϱ typically defined by discretization size. For alloys, where T_L and T_S are liquidus and solidus temperatures, the interface thickness relates to the local temperature gradient:

$$\delta \approx \frac{T_L - T_S}{|\nabla T|} \quad (27)$$

In Roy et al. (2018), simplifying Equation (21) to a phase function, the new form is:

$$\phi = \frac{1}{2}\left[\tanh\left(A\frac{T - T_M}{T_L - T_S}\right) + 1\right] \quad (28)$$

where T_L and T_S are liquidus and solidus temperatures, T_M the average, $\phi = 0$ for $T < T_S$, $\phi = 1$ for $T > T_L$, and $0 < \phi < 1$ satisfies the mushy region $T_S < T < T_L$.

2.2. Time and spatial normalization

Testing the phase-field model (Equation (21)) with Equation (27), a normalized temperature field in a 1D domain $0 \le x \le \omega$, with velocity v:

$$\frac{T - T_M}{T_L - T_S} = -3.2 + 1.6H\left[1 - \left(\frac{x - vt}{h}\right)^2\right]\left[1 - \left(\frac{x - vt}{h}\right)^2\right]^2 \quad (29)$$

where H is the Heaviside function for a region of width $2h$ with $h = 0.1\omega$. Interface thickness $\delta \approx h$. Equation (37) is non-dimensionalized by T_M/L_0, using normalized time and space dimensions $\tilde{x} = x/\omega$, $\tilde{t} = tv/\omega$. Assuming $c_S = 0.155L_0/T_M$ and $c_L = 1.11L_0/T_M$, parameters for Inconel 625 are calculated based on L_0/T_M. The computed phase distribution from Equation (29) and solving Equation (28) are shown in Figure 3a. The normalized temperature distribution at $\tilde{t} = 1$ is shown in Figure 3a. The fixed-dynamic frame capturing phase domain is the laser direction in Figure 3b.

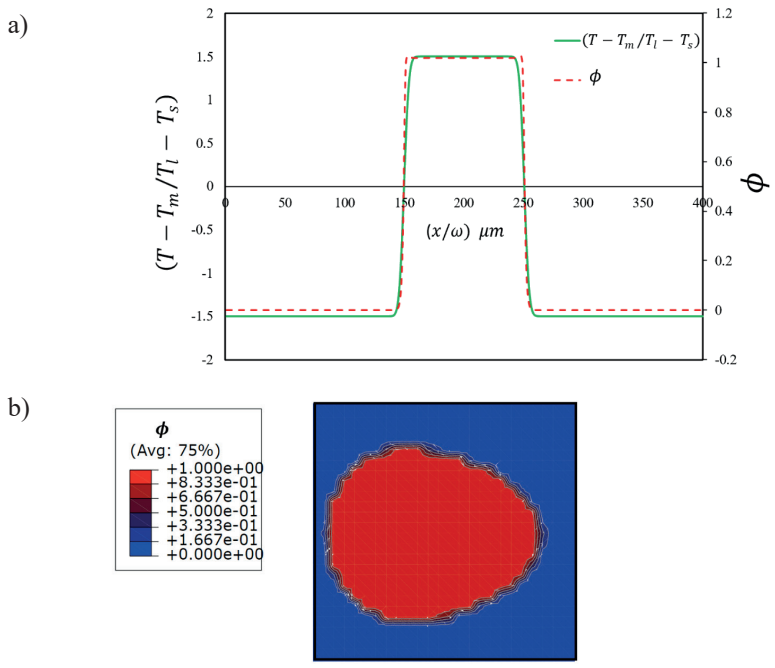

Fig. 3. Comparison of the phase parameter ϕ computed using the function from Equation (27) (phase function) and Equation (28) (phase-field) (a), with a moving temperature domain is shown (b)

2.3. Constitutive mechanical equations

The temperature history from the heat transfer analysis is applied to the mechanical model as a thermal load. Due to non-uniform expansion and shrinkage, stress and strain are generated around the melt pool domain. For an arbitrary point in the domain Ω, the equilibrium equation is given in vector form:

$$\nabla \cdot \sigma + \mathbf{b} = 0 \tag{30}$$

where σ is the second-order stress tensor and **b** is the body force vector. The total strain at any material point is related to the displacement field. AM process is generally supported using structures that greatly suppress component distortion during printing. Throughout solidification, the small deformation theory can be used to conserve computational resources. Using small deformation theory, the total strain can be written as:

$$\epsilon = \frac{1}{2}(\nabla \mathbf{u} + (\nabla \mathbf{u})^T) \tag{31}$$

where ϵ is the strain tensor, which can be decomposed into several components:

$$\epsilon = \epsilon^e + \epsilon^p + \epsilon^t \tag{32}$$

Here, ϵ^e, ϵ^p, and ϵ^t represent elastic, plastic, and thermal strains, respectively. Phase transformation-induced strain can be neglected for stainless steels like Inconel 625. Considering Hooke's law, the elastic stress decomposition is given as:

$$\sigma = D : \epsilon^e \equiv \epsilon - \epsilon^p - \epsilon^t \tag{33}$$

where D is the elasticity matrix, and elastic constants such as Young's modulus E and Poisson's ratio ν are used to determine the matrix. For isotropic materials, the elastic portion of strain is given by:

$$\epsilon_{ij}^e = \frac{1+\nu}{E}\sigma_{ij} - \frac{\nu}{E}\sigma_{kk}\delta_{ij} \tag{34}$$

where δ_{ij} is the Kronecker delta and $i, j = 1, 2, 3$. Plastic strain arises due to yielding and strain hardening. Assuming isotropic hardening in the plastic zone, the increment of plastic strain can be expressed as:

$$\epsilon_{ij}^p = d\lambda \frac{\partial f}{\partial \sigma_{ij}} \tag{35}$$

where $f = \sigma_M - \sigma_y$ is the yield function, $d\lambda$ is the proportionality factor, and σ_M, σ_y represent the Mises and yield stresses, respectively. Thermal strain can be expressed as:

$$\epsilon_{ij}^t = \alpha(T - T_{ref})J^T \tag{36}$$

where $J^T = [1\ 1\ 1\ 0\ 0\ 0]$.

2.4. Summary of the governing equations

The uncoupled thermomechanical phase-field problem described in the previous section can be represented by the summary of the strong form equations given in Table 1, constrained by initial and boundary conditions (BCs) represented in Table 2. This is under the assumption of $\Gamma_D \cup \Gamma_N = \partial\Omega$ and $\Gamma_D \cap \Gamma_N = \varnothing$, with Γ_D and Γ_N indicating the Dirichlet- and Neumann-type boundaries, respectively.

Table 1. Strong form equations governing the coupled problem

Momentum balance	$\nabla \cdot \sigma = 0$
Temperature evolution	$\frac{dT}{dt} = \frac{k(\phi)\nabla^2 T - Q}{c_s(\phi)T + p(\phi)\left[L + (c_l - c_s(\phi))(T - T_m)\right]}$

Table 2. Governing initial and boundary conditions

Dirichlet BC (Γ_D)	$\begin{cases} u(x,t) = u^*(x,t) & \text{on } \Gamma_{D_u} \\ T(x,t) = T^*(x,t) & \text{on } \Gamma_{D_T} \end{cases}$
Neumann BC (Γ_N)	$\begin{cases} -\kappa\nabla T \cdot \mathbf{n} = q & \text{on } \Gamma_{N_T} \\ \sigma \cdot \mathbf{n} = t^* & \text{on } \Gamma_{N_u} \end{cases}$
Initial conditions	$\begin{cases} T = T_{ref} & \text{on } \Gamma_{N_T} \\ u = \bar{u} & \text{on } \Gamma_{N_u} \end{cases}$

2.5. Numerical implementation

The FEM is utilized to implement the formulation outlined in the previous section by using the weak form of the governing PDEs given in Table 1. To this end, arbitrary test functions associated with the field variables are employed and are multiplied by their respective PDEs, generating the weak forms as detailed below:

$$\int_\Omega \sigma : \nabla \delta u \, d\Omega = 0 \tag{37}$$

$$\int_\Omega \delta T \frac{\partial T}{\partial t} d\Omega = \int_\Omega \nabla \delta T \cdot \frac{k(\phi)\nabla^2 T}{c_s(\phi)T + p(\phi)\left[L + (c_l - c_s(\phi))(T - T_m)\right]} d\Omega - \int_\Omega \delta T \frac{Q}{c_s(\phi)T + p(\phi)\left[L + (c_l - c_s(\phi))(T - T_m)\right]} d\Omega \tag{38}$$

Using the standard FEM method, the field variables and their spatial derivatives are approximated at the element level as:

$$u = N_u u_e, \quad \epsilon = B_u u_e, \tag{39}$$

$$T = N_T T_e, \quad \nabla T = B_T T_e, \tag{40}$$

where u_e, and T_e are the nodal values of the displacements, and temperature at an element e. For interpolation

purposes, the standard shape function matrices N_u, N_T and their corresponding gradient operators B_u, B_T are utilized. Based on the above relations, the weak forms presented in Equations (39) to (40) can be rearranged based on Equations (41) and (42), yielding the following residuals:

$$r_u = \int_\Omega \sigma B_u^T \, dV - \int_{\Gamma_{N_u}} t^* N_u^T \, dS \tag{41}$$

$$\begin{aligned} r_T = &- \int_{\Gamma_{N_T}} \left[c_s(\phi) N_T T_e + p(\phi)(L + (c_l - c_s(\phi))(N_T T_e - T_m))\right] \\ &\times k(\phi)\left[B_T\right]^T \left[N_T\right] dS + \int_\Omega \left[c_s(\phi) N_T T_e + p(\phi)(L + (c_l - c_s(\phi))\right. \\ &\left.\times (N_T T_e - T_m))\right] k(\phi)\left[B_T\right]^T \left[B_T\right] dV + \int_\Omega Q\left[N_T\right]^T dV = 0 \end{aligned} \tag{42}$$

where r_u and r_T are, respectively, the residuals associated with the displacement field and temperature field.

2.5.1. ABAQUS procedure

The implementation of the heat transfer analogy in ABAQUS utilizes the user thermal behavior of materials (UMATHT). This approach operates at the integration point level with built-in temperature elements like the DC3D8 (Hex-8 linear heat transfer) type. Initially, global variables in the UEXTERNALDB user subroutine are initialized. A solution-dependent state variable (SDV) is assigned to track the material state as the powder phase at a specific time. Upon application of heat through the DFLUX subroutine, this SDV transitions to one. Once cooled, the SDV remains fixed at one, signifying fully solid material properties. Continuum-scale material addition is facilitated by the UEPACTIVATIONVOL subroutine, which interprets event series information for material deposition via the moving laser. At the end of each increment, the UMATHT subroutine reads the temperature at each material point and updates the consolidation value for points meeting the state change criterion. The derivative of internal energy with respect to temperature incorporates phase-field variables, including the enthalpy function, to account for latent heat effects due to phase fractions. The USDFLD subroutine manages material states at the end of each time increment and stores them. Additionally, the FILM and RADIATE subroutines apply heat boundary conditions for convection and radiation, respectively. ABAQUS uses load type labels FFS and RFS to automatically define thermal loads for film coefficient and radiation at open faces of activated elements, addressing iterative changes in convective and radiative boundary conditions during element activation. Information transfer between subroutines is facilitated by COMMON blocks, detailed in Figure 4.

Algorithm 1 Thermal Modelling

procedure UEXTERNALDB
  if LOP=0 **then**
    Initialize the set of state variables at time t_0
    Solid State : $\varphi = 0$
    Powder Material : $\psi = 0$
  end if
end procedure
procedure UEPACTIVATIONVOL
  Element activation for mass rate
end procedure
procedure DFLUX
  Apply the volumetric heat flux for laser heat source:
  $U(x, y, z, t) = \frac{fP}{\pi r_l^2} exp(-f\frac{x^2+(y-v)^2}{r_l^2})$
end procedure
procedure UMATHT
  Transfer heat source by common block from DFLUX
  Update the state variables for φ and ψ
  Set the material properties depends on temperature:
    $k(\psi) = (1-\psi)k_p + \psi k_d$
    $C_s(\psi) = (1 - \epsilon_0(1-\psi))C_d$
  Using the Galerkin weighted residual method to obtain the classical integral form to solve the non-linear thermal equations:
    Internal thermal energy (enthalpy) for unit of mass: e
    Derivative of internal energy with respect to temperature: $\frac{de}{DT}$
    Heat flux vector with respect to temperature: $\hat{q} = -k(\psi)\nabla(T)$
    Variation of heat flux vector to temperature: $\frac{\partial \hat{q}}{\partial T}$
    Variation of heat flux vector to the spacial gradient of temperature: $\frac{\partial \hat{q}}{\partial \frac{\partial T}{\partial x}}(i = 1, 2, 3)$
end procedure
procedure USDFLD
  Transfer state variables by common block from UMATHT
  Store state variables and go to the next time increment
end procedure

Fig. 4. User subroutines algorithm for the implementation of diffusive phase function model in phase changing exploiting the analogy with heat transfer

The system of equations is implemented in ABAQUS through user coding in the FORTRAN language, combining activation element regimes with the UEPACTIVATIONVOL subroutine and predefined temperature fields from thermal analysis. The UEXPAN user interface, as depicted in Figure 5, is integrated into the procedure for calculating thermal strains. The UMAT subroutine is invoked at all material points to perform constitutive model integration (also known as local integration or stress update algorithm) and returns updated stress and Jacobian. Notably, this procedure employs built-in structural elements such as the C3D8 (Hex-8 linear brick element) type (see Fig. 5).

Algorithm 1 Mechanical Modelling

procedure USDFLD
  Transfer state variables by common block from UMATHT
  Store state variables and go to the next time increment
end procedure
procedure UEPACTIVATIONVOL
  Element activation for mass rate
end procedure
procedure UEXPAN
  Calculate $\epsilon_{thermal} = a(T)_i T$
end procedure
procedure UMAT
  Solve [K]du = dF
  update u=u+du
  Recalculate strain and stress:
  $\epsilon = Bu$
  $\epsilon_{elastic} = \epsilon - \epsilon_{plastic} - \epsilon_{thermal}$
  $\sigma = E\epsilon_{elastic}$
  if $\sigma > \sigma_{Yield}$, then $correct$
  $\epsilon_{plastic}, \epsilon_{elastic}, and \ \ \sigma$
  Assemble nodal force {dF}
end procedure

Fig. 5. User subroutines algorithm for the implementation of thermo-elastoplastic material framework

3. Numerical examples

In this section, numerical models are adopted to study Inconel 625 across various computational scales. The investigation begins at the single-track scale, focusing initially on melt pool temperature, morphology, and subsequently on induced residual stresses and strains. High-fidelity discretization resonances in meso-scale for the single track(s), a lumped computational model including thermal and mechanical are developed for multi-layer deposition process. The macro scale model focuses on the effect of re-melting and re-solidifications on the consequent residual stress, strains.

3.1. Single-track scale

For model calibration, the limited number of cladding lines from Inconel 625 powder were printed by various laser powers, scanning speeds, and feed rates to investigate the capability of the model in predicting the melt pool morphology. Then, the mechanical-based simulations were carried out by resorting to the thermal loads to study the residual stress and distortion. Figure 6 shows how the computed material state variables work with time and temperature, the red and blue colors denote the liquid phase and solid phase, respectively and the mushy area located between these boundaries in the color contour, in Figure 7 melt pool size for cladding a single track of Inconel 625 on the substrate for different deposition relies on changing the laser power. The results in Figure 8 show the comparison between the experimental from (Darabi et al., 2022) as mentioned in Table 4, and obtained results from FEM simulations for the dimension of melt pools, including the height, width, and depth values with process parameters from Table 3. It can be seen that the proposed model can predict the melt pool dimension with reasonable accuracy.

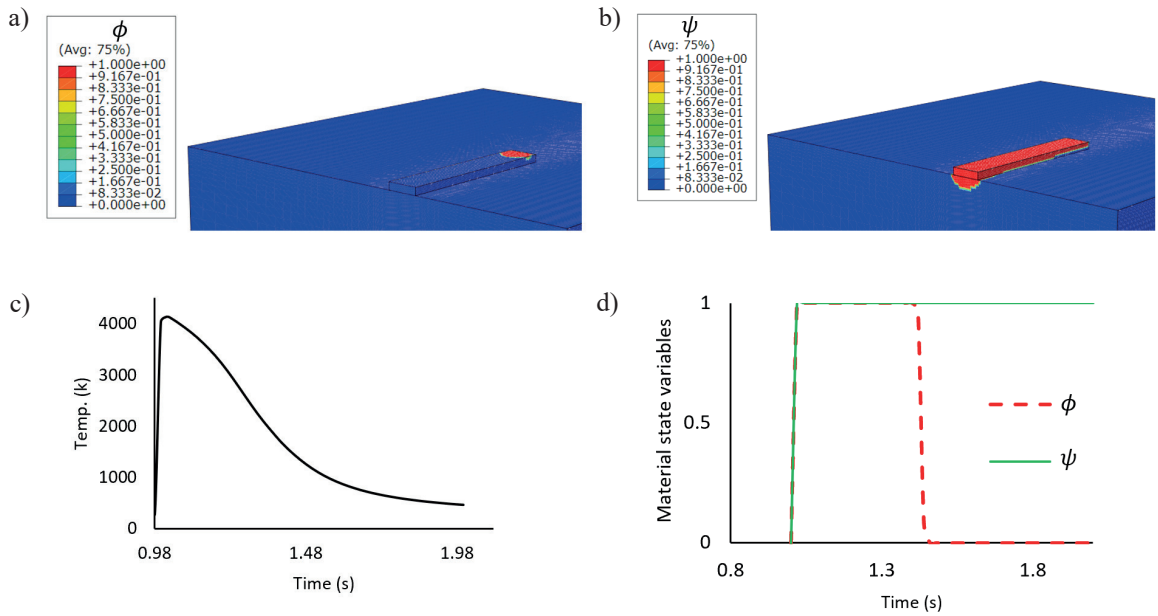

Fig. 6. Material state variables: a) phase parameter ϕ; b) consolidation parameter ψ; c) temperature profile at a point on the top of the coating surface; d) variation of material state variables with time for the same point on the top. All results are for P = 2 kW, v = 10 mm/s, F = 10 gr/min

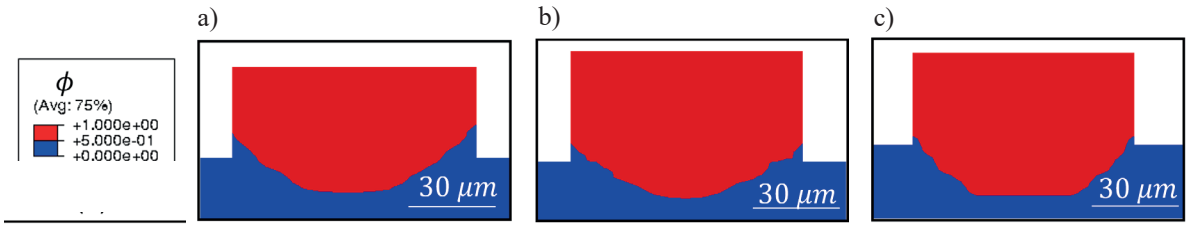

Fig. 7. Predicted melt pool morphology in the Z direction for single-track with SS = 10 mm/s, FR = 10 gr/min: a) P = 1.5 kW; b) P = 2 kW; c) P = 2.5 kW

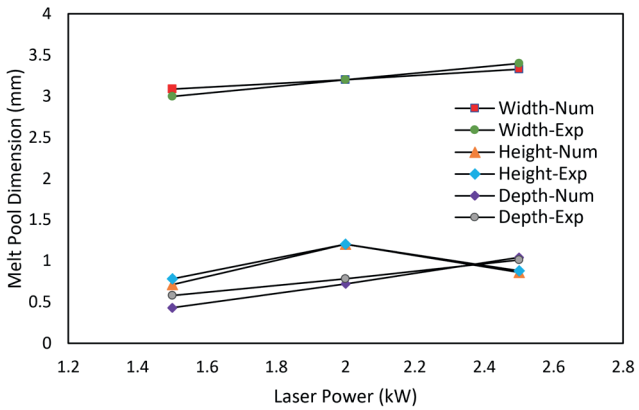

Fig. 8. Comparison of the predicted melt pool width with the experimental results from (Darabi et al., 2022)

Table 3. Thermo-physical properties of the material of cladding and substrate

Property	Value
T_s [K]	1563
T_l [K]	1723
C_s [kJ/kg]	4.2e5
C_l [kJ/kg]	3.01e6
L_f [kJ/kg]	44.34

Table 4. List of process parameters for the single-track scanning process

Description	Value
Laser power [kW]	P = 1.5, 2, 2.5
Laser scanning speed [mm/s]	v = 10
Powder feed rate [g/min]	F = 10
Laser beam radius [mm]	r_l = 1.25

3.1.1. Thermal stability analysis

The dynamics of transient heat transfer are commonly analyzed using numerical time integration schemes, such as explicit and implicit methods. Time-dependent variables are discretized using finite difference techniques with a time increment to estimate continuous field variables at subsequent time points. By choosing different finite difference schemes (e.g., forward or backward finite difference), one can obtain explicit or implicit integration schemes. In this study, the implicit method (backward finite difference) is utilized due to its unconditional stability. Although implicit integration is theoretically stable for any chosen time step, practical limitations arise due to considerations of numerical convergence and computational accuracy. Specifically, the time step must satisfy the Courant–Friedrichs–Lewy (CFL) condition for numerical stability. The CFL condition is represented by $C = |\mathbf{v}|\Delta t / \Delta l$, where $|\mathbf{v}|$ is the magnitude of the velocity vector (here, the velocity of the laser beam affecting mass fraction equations), Δt is the time increment, and Δl is a characteristic element length in the direction of flow. Heat cannot be convected across more than one element length Δl within a single time increment. Figures 9 (a, b) illustrate the transient temperature profiles at a specific point using different mesh sizes and time steps. Figure 9a shows results for a mesh size of 0.2 mm and a time step of 0.02 s, while Figure 9b depicts results for the same mesh size but with a smaller time step of 0.001 s, highlighting the importance of adhering to the CFL condition. When the CFL number is less than 1, spurious oscillations in the temperature versus time curve can occur, even when using automatic time incrementation in the solver to ensure convergence, necessitating additional considerations. The Peclet number, another dimensionless parameter indicating the dominance of convection over mass addition in the computational domain, also needs careful consideration in additive manufacturing process modeling, particularly at high fidelity levels. Figures 9 also displays the number of iterations required for convergence in each time increment, superimposed on the temperature versus time response.

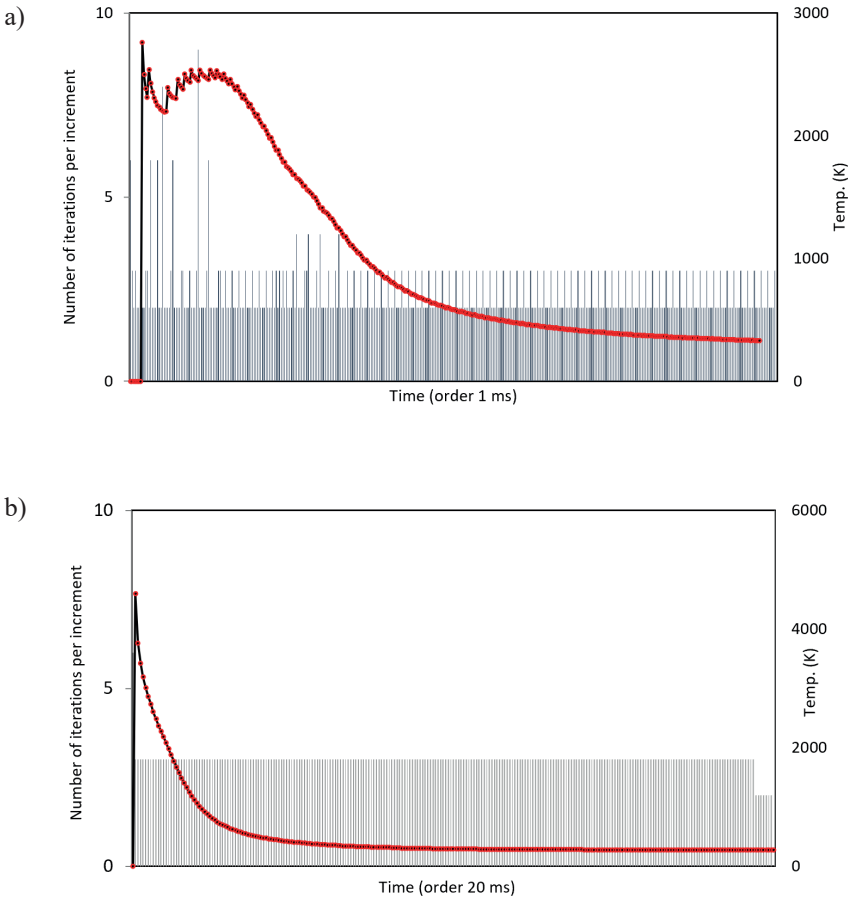

Fig. 9. Transient temperature solution for a single track, showing the number of iterations per increment, with the temperature versus time curve superimposed:
a) mesh size 0.02 mm and time increment 0.001 s; b) mesh size 0.02 mm and time increment 0.02 s

3.1.2. Characteristics of melt pool

The unique microstructures in additive manufacturing (AM) processes are influenced by localized high thermal gradients and rapid cooling rates during solidification. Figure 10a illustrates the temperature distribution profiles versus the distance from the head to the tail of a melt pool domain. In the axisymmetric view, cooling rates are shown within the same time frame and calculation context. Near the center of the melt pool, within the molten isotherm domain, the cooling rate approaches zero. At the head of the melt pool where new mass is added (powder particles), a positive cooling rate is observed due to the mixture of powders and substrate (mushy zone $0 < \psi < 1$). Conversely, at the tail of the melt pool, a negative cooling rate indicates the initiation of solidification. The computational model used assumes heat transfer occurs solely through heat conduction (Fourier's law), termed a conductive model, without accounting for fluid flow induced by surface tension gradients in the melt pool. The temperature gradient in the direction perpendicular to the laser movement leads to the Marangoni effect, where fluid motion is primarily driven by surface tension gradients induced by temperature gradients. This phenomenon determines the width of the melt pool. Depending on whether the temperature of the liquid metal at the top of the melt pool is higher or lower than at the bottom, the melt pool exhibits upward or downward movement. Figure 10b demonstrates that localized laser heating of the plate surface and melting of the top cladding layer results in the highest temperatures at the center of the melt pool, decreasing radially (in the x direction), thereby creating a surface tension gradient in the melt pool and inducing outward or inward melt flow. The maximum boundary indicates the width of the melt pool morphology.

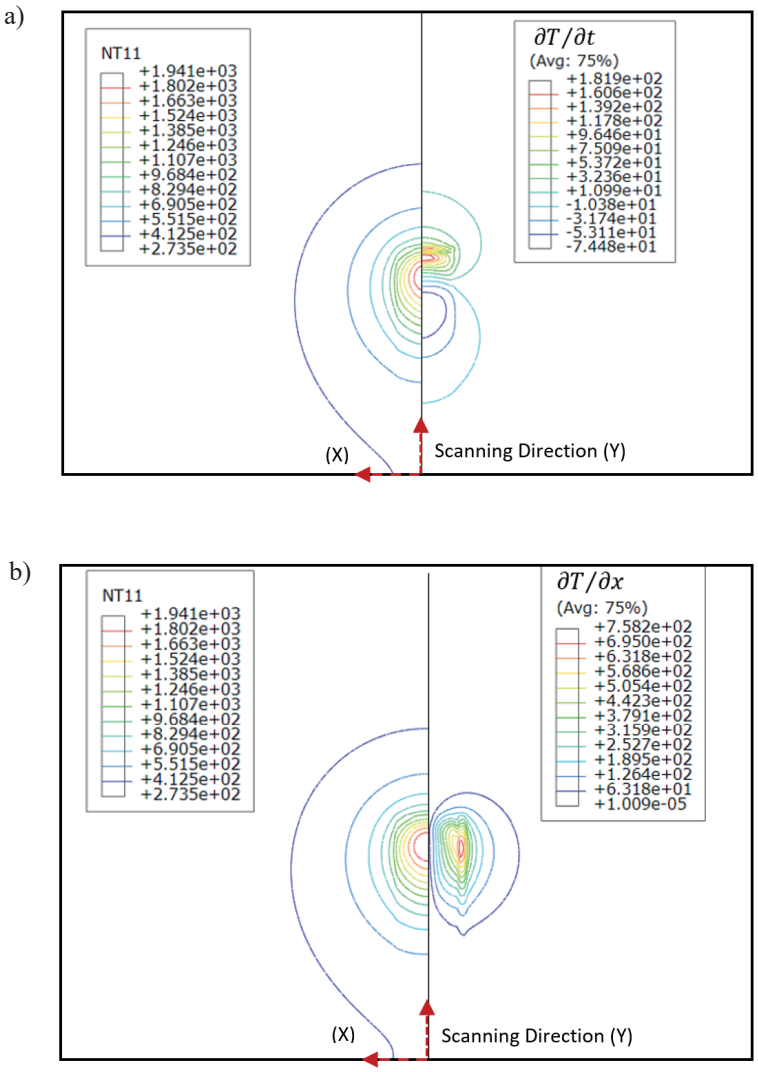

Fig. 10. Top surface temperature sequence during AM process:
a) axisymmetric temperature view vs cooling rate taken at the same time frame;
b) axisymmetric temperature view vs temperature gradient taken at the same time frame

3.1.3. Effect of phase change on enthalpy

Here, the phase change problem, specifically melting and solidification during the deposition in the AM process, is addressed. The domain encompasses phases transitioning between powder and molten or molten and solid, separated by distinct interfaces. Two primary models, the sharp interface and diffusive interface models, are employed to describe these phase changes, as depicted in Figure 11a and b. In the sharp interface model, solid and liquid phases are assumed to be separated by an infinitely thin interface defined by temperature. However, this singularity poses challenges for numerical simulations in Lagrangian space. Alternatively, in a Eulerian framework, explicit interface tracking schemes using level set functions (Zhang et al., 2018) can be employed to address this issue. Our approach utilizes a model where phase change occurs across an extended interface domain with finite thickness, incorporating a latent heat model. The transition between phases is detailed in Section 2, and the impact of phase function steepness is illustrated in Figure 11b. Our proposed model employs a broader transition region to mitigate nonlinearities observed in the AM process. Figure 11b demonstrates that, in Lagrangian space, as A approaches infinity, a sharp transition condition can be approximated using a diffusive function based on Equation (28). Figure 12 presents the enthalpy function extracted from ABAQUS, where the slope represents the specific heat capacities for the liquid and solid phases, and L_f denotes the latent heat of fusion. In the mushy region, an average of the respective specific heat values is utilized. These values are derived from (Darabi et al., 2022).

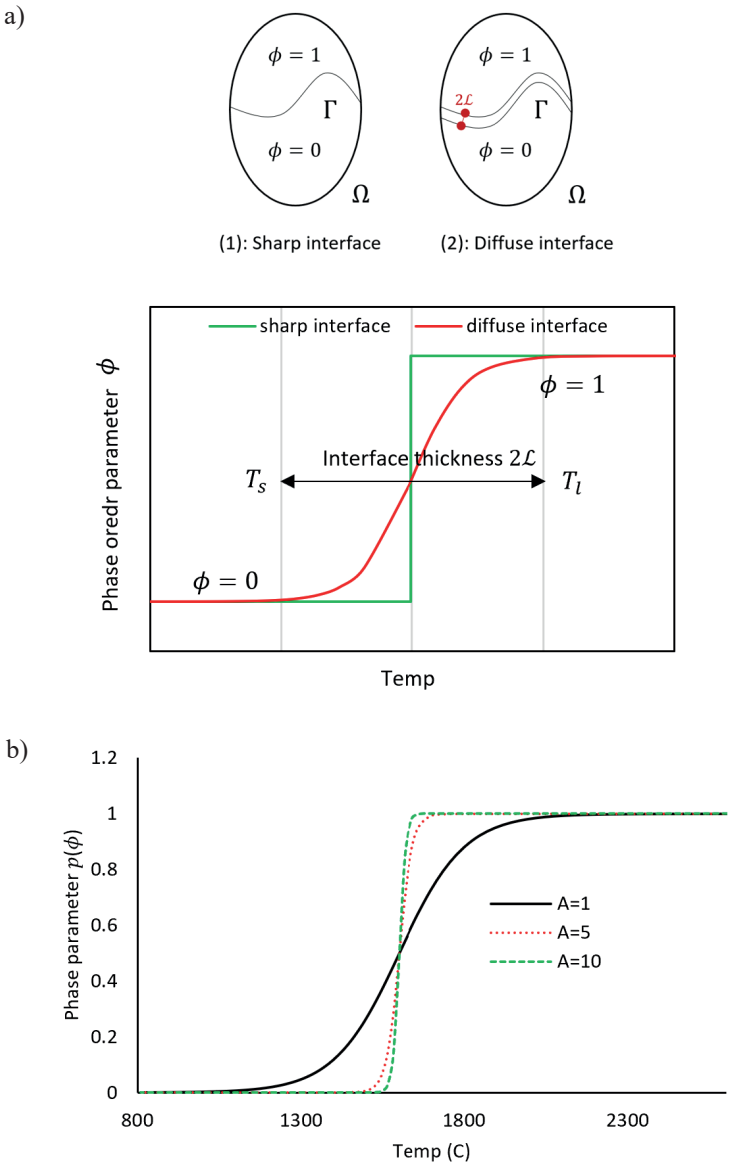

Fig. 11. Phase transition: a) two approaches, sharp interface and diffusive interface, with the phase field function ϕ in the temperature domain; b) effect of transition sharpness in the interpolation of the phase function

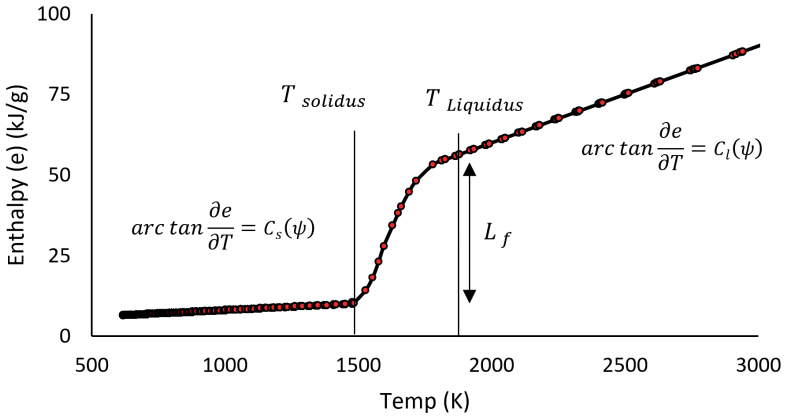

Fig. 12. Temperature-dependent specific enthalpy for material point in ABAQUS

3.1.4. Residual stress and strain

The thermal history obtained from the heat transfer analysis is used to evaluate residual stress and strain distributions over time in the mechanical analysis. The UEPACTIVATIONVOL subroutine handles element activation, while the UMAT user interface incorporates temperature-dependent material definitions to capture temperature and plastic strain rate evolution post-yielding. The temperature-dependent material properties for Inconel 625 in solid state are shown in Figure 13. For powder and liquid states, the material stiffness is considered negligible compared to the dense solid state, with a value set to 0.1 GPa to ensure a positive definite stiffness matrix while virtually deactivating stiffness. At the melting temperature, a negligible yield stress of 0.1 MPa with perfect plasticity is set to simulate the annealing effect (resetting equivalent plastic strain to zero to eliminate hardening memory) (Muránsky et al., 2015). Controlling the time increment for thermal analysis is described in section 3.1.1; for mechanical analysis, a time increment five times larger than the thermal increment is used to conserve computational resources. The rapid temperature decrease post-solidification minimally affects stress evolution due to the low modulus at high temperatures. State variables updated and saved in the previous thermal analysis using the USDFLD subroutine (detailed in section 2.5.1) are employed as additional field variables to apply state-dependent elastic and plastic properties. The UEXPAN user interface defines isotropic thermal strains considering temperature and the coefficient of thermal expansion, as presented in Figure 13c.

Figure 14 illustrates the evolution of transverse and longitudinal stresses at midpoint P of the cladding against temperature. During the initial laser cladding stages, the coating expands due to heating, inducing compressive longitudinal stresses and tensile transverse stresses. As the cladding melts, both stresses approach a near-zero state until solidification begins, initiating the development of compressive stresses around 0.45 s. Upon complete cooling, longitudinal and transverse stresses stabilize at approximately 665.63 MPa and 166.8 MPa, respectively.

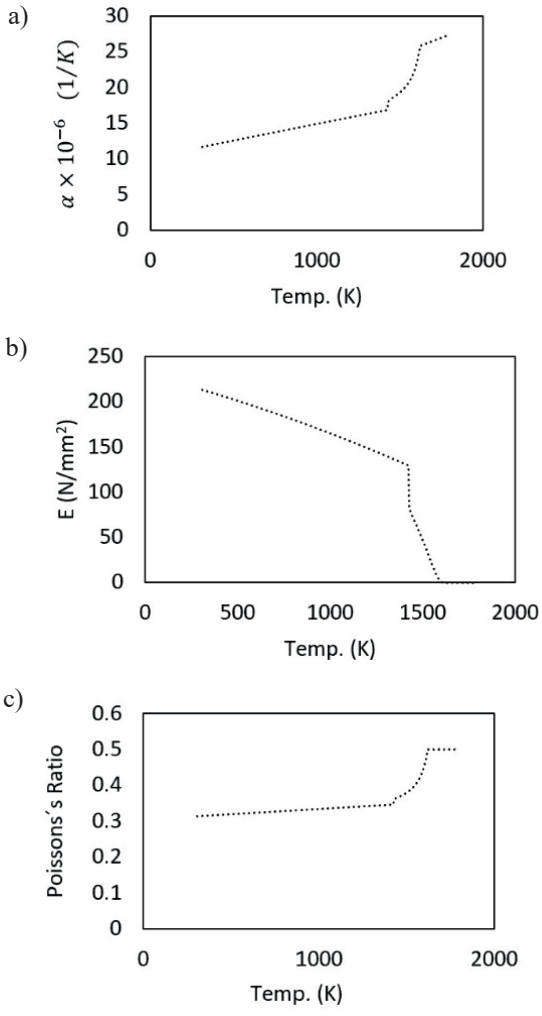

Fig. 13. Inconel 625 material properties depending on temperature: a) coefficient of thermal expansion; b) elastic modulus; c) Poisson's ratio

Figure 15 displays transverse, longitudinal, and equivalent Mises residual stresses for the single track computational domain. In triple cases, maximum tensile stresses range from 800 MPa to 900 MPa, with compressive stresses around −700 MPa. Transverse compressive stress in the substrate center results from shrinkage induced by cladding solidification (Fig. 15a), a well-documented factor contributing to induced cracking (Szost et al., 2016; Tian et al., 2020).

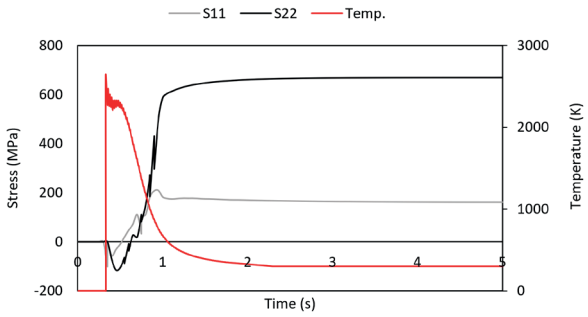

Fig. 14. Stress evolution at midpoint P: transverse stress (S11) and longitudinal stress (S22) over time with temperature distribution

a)

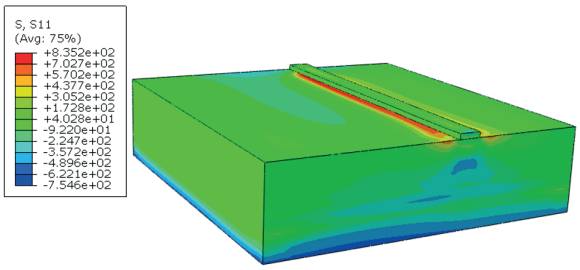

b)

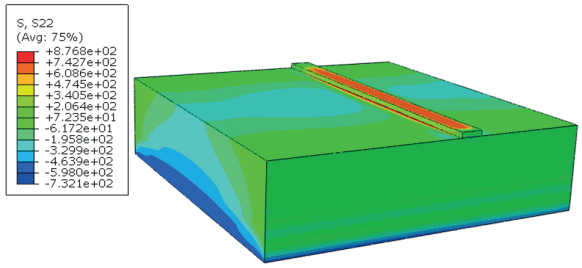

c)

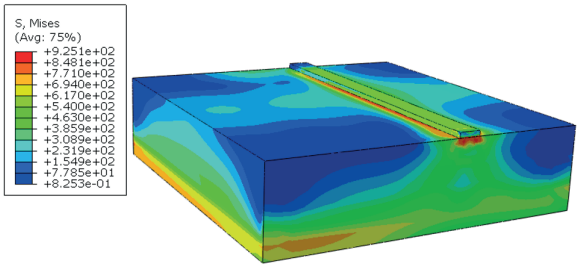

Fig. 15. Residual stress distribution: a) transverse stress (S11); b) longitudinal stress (S22); c) equivalent Mises stress

Figure 16 illustrates longitudinal, transverse, and radial stress distributions along a cross-sectional view. Stress trends show a decrease from the coating's top towards the substrate's top surface, transitioning from tensile to compressive ranges. Notably, maximum tensile stresses occur at the substrate-cladding junction.

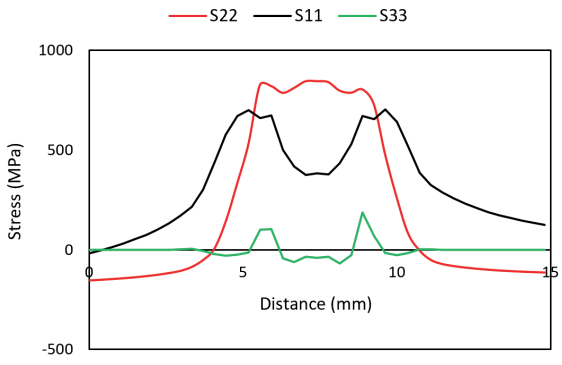

Fig. 16. Longitudinal, transverse, and radial stress distribution along a cross-sectional view

3.2. Multi-layer scale

3.2.1. Thermal prediction at the multi-layer scale

In this section, a thermal simulation of a multi-layer structure is conducted to fabricate a thin-walled structure, aiming to obtain maps of temperature, cooling rate, and phase-field parameters for finite element nodes. The extension from single-layer modeling to multi-layer modeling includes considerations of re-solidification, which are crucial for further studies on residual stresses. As the laser source moves, metallic powders are simultaneously injected into the laser beam by surrounding nozzles, rapidly heating local points to their maximum values. Material is added layer-by-layer and solidifies from the melt pool, creating new features. The phase history defined by local temperatures in the Directed Energy Deposition (DED) process is illustrated in Figure 17. Material states are tracked using state variables including ϕ and ψ: ϕ, $\psi = 0$ denote the powder state, $\psi = 1$ represents a fully consolidated state, and the mushy region $0 < \psi < 1$ exists between powder and liquid phases. Heat flux melts the material ($\phi = 1$) and it solidifies upon cooling ($\phi = 0$). Both liquid and bulk solid states are treated as $\psi = 1$. Figure 17c shows the evolution of porosity within the melt pool, which decreases after solidification; ε represents the macroscopic porosity value varying with temperature. It is noted that a lumped resolution is used in the multi-layer model to save computational costs, emphasizing phase change and material status for accurate process modeling. Figure 18 presents the transient temperature fields and state variables at points of

interest A and B within the fabricated thin-walled structure. Sharp temperature peaks indicate rapid heating and cooling cycles associated with laser scanning over these points. Point A exhibits lower peak temperatures compared to point B, attributed to heat accumulation during the deposition of middle layers.

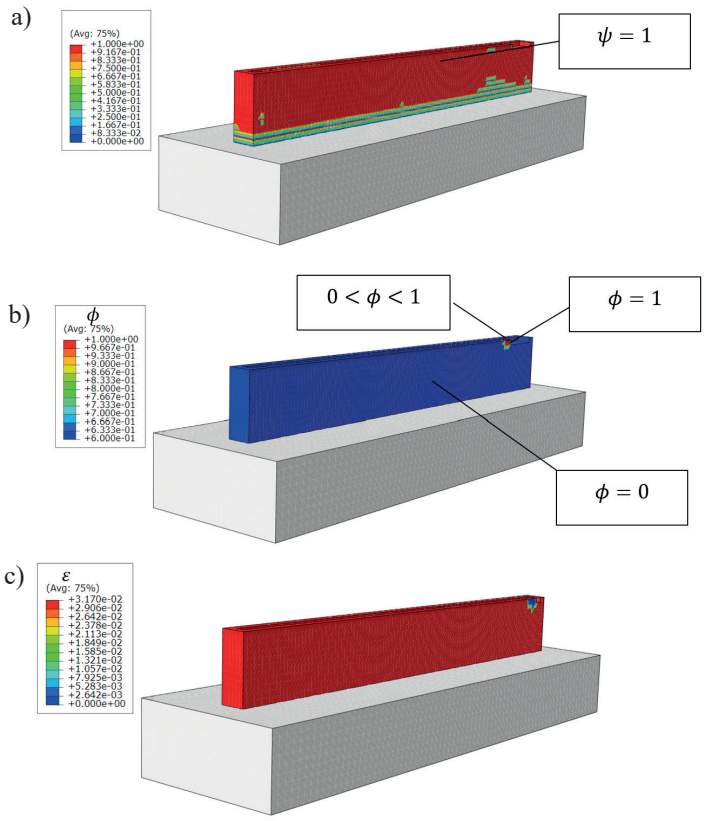

Fig. 17. Prediction of phase domains in in-situ printing of the thin-walled structure: a) consolidation control to record history of melted FE nodes; b) liquid to fully solid phases for FE nodes; c) evolution of porosity

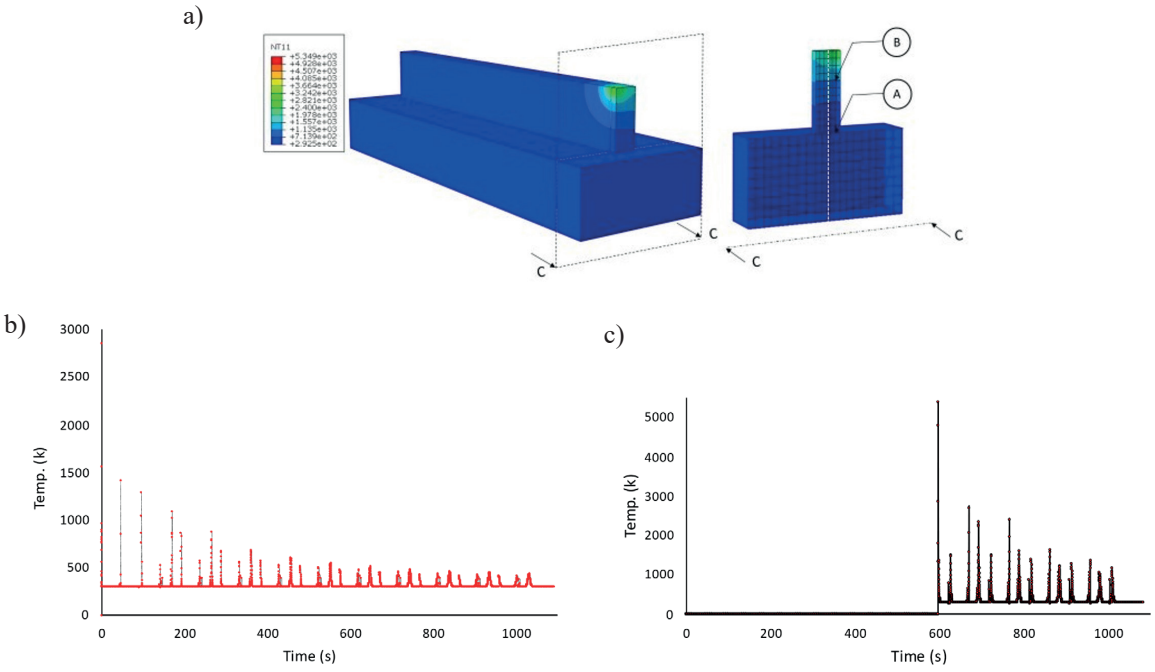

Fig. 18. Transient temperature field and state variables for point of interest A: a) temperature contour in the thin-walled structure and sectional view around Point A; b) temperature vs. time for Point A; c) temperature vs. time for Point B

3.2.2. Residual Stress Prediction in the Multi-Layer Scale

Building upon single-layer residual stress considerations, this section predicts residual stresses and distortions in a multi-layer case study. An uncoupled mechanical simulation, leveraging thermal responses, is employed. Unlike the variable number of elements used in single-layer simulations across the coating height, a single element is dedicated to the entire layer thickness based on findings from previous research (Bayat et al., 2020; Peng et al., 2018; Williams et al., 2018). Thermal history investigation reveals the strongest gradients near the heat source, resulting in non-symmetrical thermal profiles and high cooling rates during solidification. Residual stresses originate from thermal expansions between irradiated material and the surrounding substrate during phase change. Figure 19 depicts the three-dimensional stress components, including σ_{11} and σ_{22}, at various stages of the deposition process: after the first layer deposition, at 50% and 75% of the building height, and upon completion of the thin-walled structure. σ_{11} and σ_{22} represent the transverse and longitudinal stress components in the *X* and *Y* directions, respectively. Regions in the powder and liquid states exhibit lower stresses compared to those in the solid state. Throughout the process, the top surfaces predominantly experience minor tensile stresses, while the bottom surface of the substrate undergoes the highest compressive stresses. Thinner substrates may experience higher residual stresses due to greater constraints from the bottom surface. There is a transition from tensile stresses at the topmost layers to compressive stresses near the coating-substrate junction. The transverse stress in the first layer shows the strongest gradient at the interface between the part and substrate, shifting towards the middle of the structure. The longitudinal stress is highest on the exterior surface and transitions towards the middle near the bottom during fabrication.

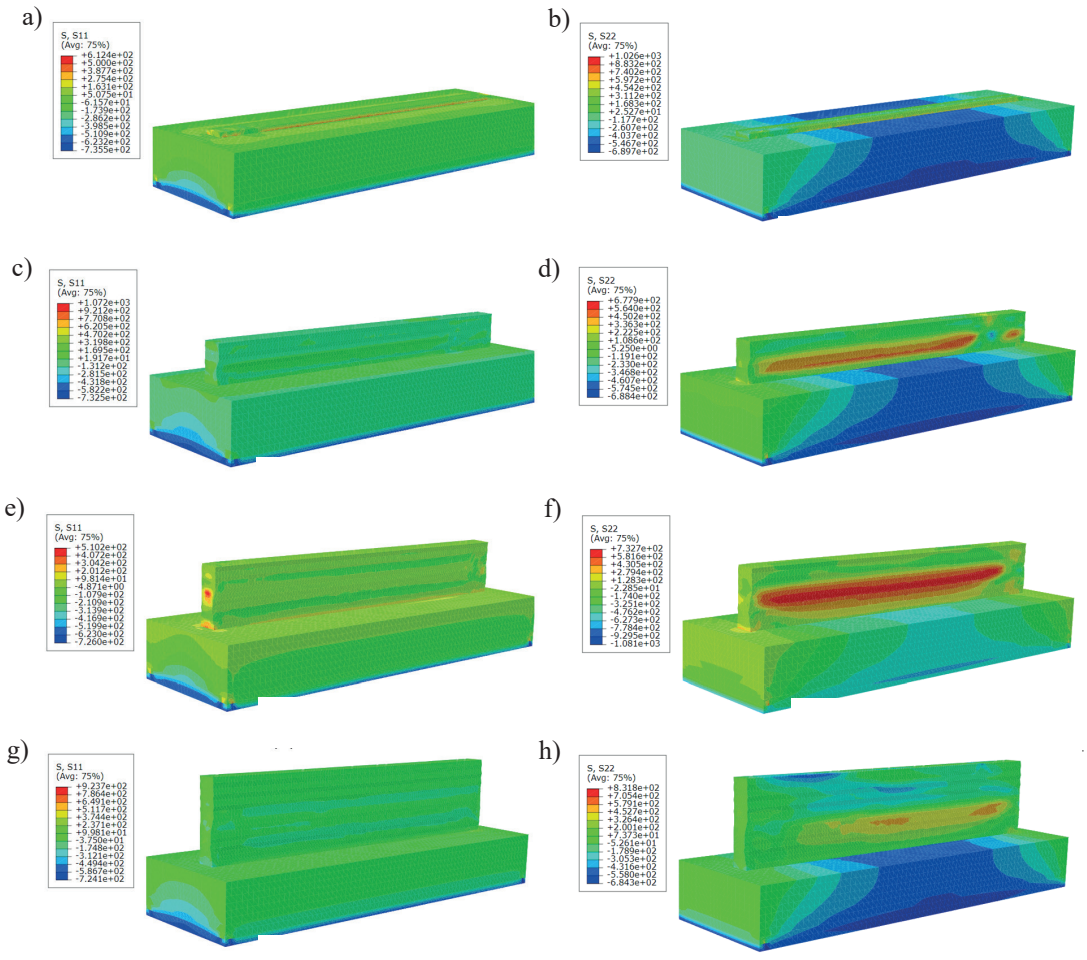

Fig. 19. Stress distribution throughout the fabrication of the thin-walled layer. Subfigures depict: a) transverse stress in the first layer; b) longitudinal stress in the first layer; c) transverse stress at 50% of the height; d) Longitudinal stress at 50% of the height; e) transverse stress at 75% of the height; f) longitudinal stress at 75% of the height; g) transverse stress at full height; h) longitudinal stress at full height. All stress values are in megapascals

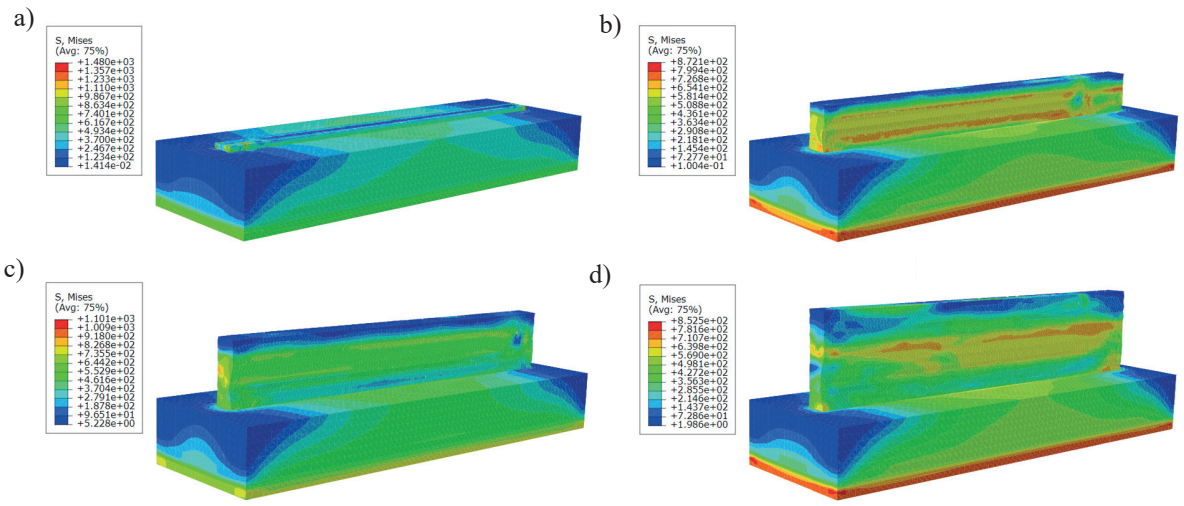

Fig. 20. Simulated von Mises stress distribution throughout the fabrication of the thin-walled layer. Subfigures depict: a) first layer; b) 50% of the height; c) 75% of the height; d) full height. All stress values are in megapascals

Figure 20 illustrates the evolution of von Mises stresses throughout the fabrication process. Peak stresses are observed at the substrate bottom and decrease towards the top surface upon completion of the thin-walled structure. Figure 21 provides a detailed view of predicted residual stress components along the centerline of a cross-section through the middle of the thin-walled structure, from the bottom interacting with the substrate to the top layer after cooling. Longitudinal stresses exhibit more significant deformation effects compared to the other components, suggesting that reducing longitudinal stress effects could mitigate deformations.

In comparison to Figure 18, the temperature history for points A and B in the first layer near the external surface and in the middle of the structure indicates that heat accumulation increases peak temperatures in the middle layers. Consequently, stiffness decreases in these layers due to higher temperatures, resulting in continuous increases in displacement from the bottom to the middle layers, stabilizing near the topmost layers. Figure 22 shows total displacement throughout the fabrication of the thin-walled structure, highlighting maximum displacement near the substrate-middle due to repeated melting and solidification cycles in the middle layers. Figure 23a compares deformed and undeformed edges induced by thermal and mechanical loads in the thin-walled structure, showing transverse sectional and longitudinal/top sectional views. Notably, taller thin-walled structures are more susceptible to deformation than shorter ones, emphasizing the importance of robust design procedures for thickness, height, and scan trajectory optimization.

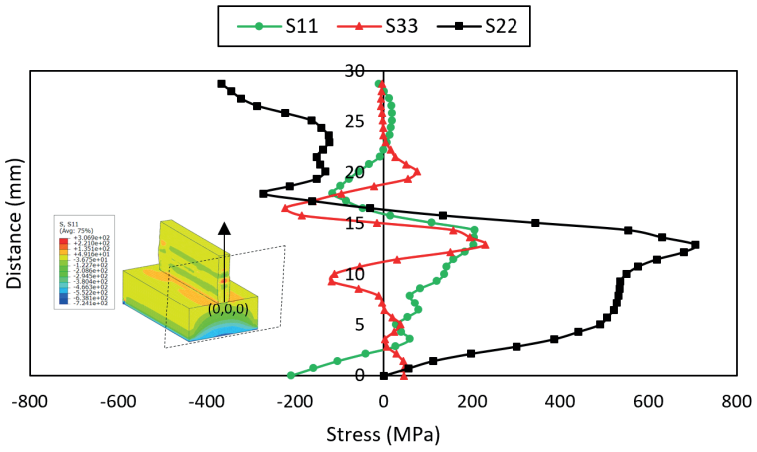

Fig. 21. Comparison of deformed and undeformed edges of the thin-walled structure induced by thermal and mechanical loads: a) transverse sectional view; b) longitudinal and top sectional views

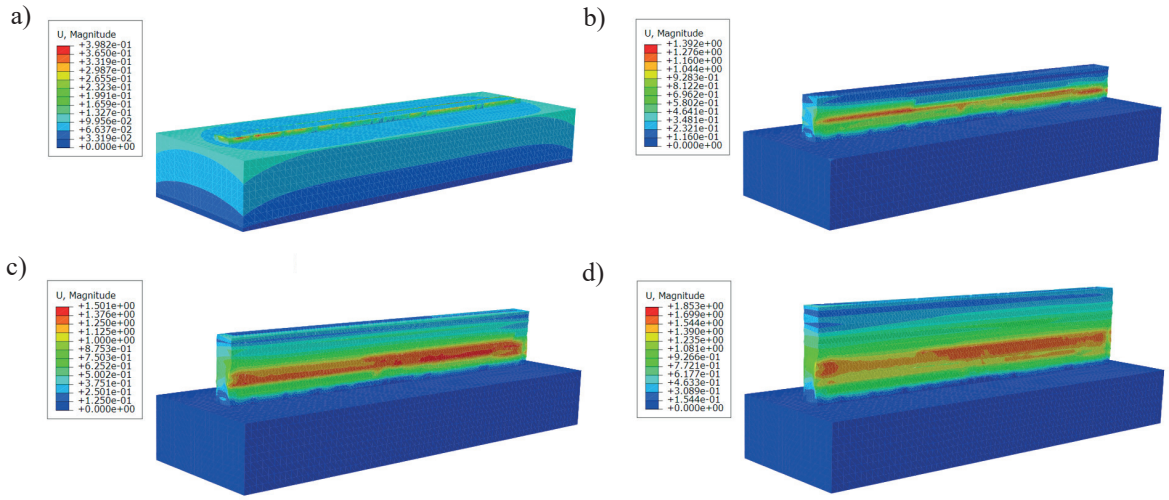

Fig. 22. Total displacement throughout the fabrication of the thin-walled layer, showing: a) at the first layer; b) at 50% of the height; c) at 75% of the height; and d) at full height. All displacement values are in millimeters

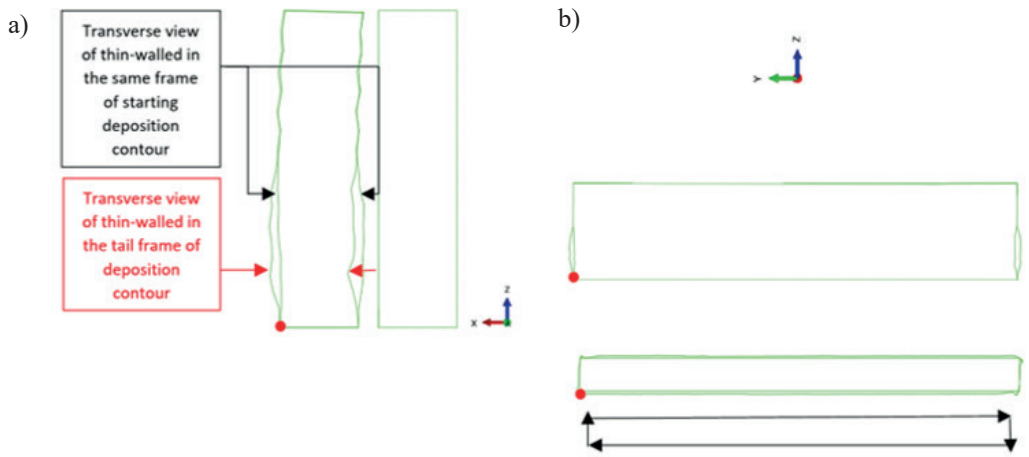

Fig. 23. Comparison of the deformed and undeformed edges of the thin-walled structure induced by thermal and mechanical loads. Panels show: a) transverse sectional view; b) longitudinal and top sectional views

4. Summary

In this study, an in-depth investigation into the additive manufacturing (AM) process was undertaken through a rigorous three-dimensional sequentially coupled thermo--mechanical analysis, with a particular focus on phase transformation dynamics and their implications. The AM process involves intricate interactions between thermal energy deposition, phase changes (solidification), and subsequent mechanical responses, making it inherently nonlinear and challenging to simulate accurately. To address these challenges, a novel numerical method was developed based on the solidification models proposed by Penrose & Fife (1990) and extended by Wang S.-L. et al. (1993). These models were adapted to incorporate both phase field and large domain phase function approaches. This hybrid approach allowed us to precisely simulate the transition between solid and liquid states during material deposition and solidification. A significant contribution of our study was the introduction of an irreversible consolidation parameter. This parameter played a crucial role in modeling the transformation of powdered material into a solid state, capturing the material's evolution throughout the heating, melting, and cooling phases. By accurately tracking these phase changes, residual stresses and deformation patterns induced by thermal cycling during the AM process were predicted. Furthermore, the evolution of porosity as a function of temperature was investigated. Since porosity is a critical factor affecting the mechanical properties of AM parts, insights were provided into how temperature variations influence the

formation and reduction of porosity within the material structure. These findings highlight the importance of advanced numerical techniques and precise modeling in optimizing AM processes. By integrating detailed phase change modeling with mechanical analysis, we sought to obtain an enhanced understanding and control of manufacturing parameters with the goal of minimizing defects and improving the mechanical integrity of fabricated components. Overall, this research contributes to the broader goal of advancing additive manufacturing technology, enabling more efficient and reliable production of complex geometries with tailored mechanical properties. The insights gained pave the way for future developments in optimizing process parameters and materials selection for diverse industrial applications.

Acknowledgments

R. Darabi gratefully acknowledges the funding provided by Fundação para a Ciência e a Tecnologia (FCT), Portugal, under the Grant number 2021.08685.BD. Additionally, she acknowledges funding of the project Hi-rEV – Recuperação do Setor de Componentes Automóveis under the program PRR – Plano de Recuperação e Resiliência – Agendas Mobilizadoras funded by Agência para a Competitividade e Inovação.

References

Alart, P., Maisonneuve, O., & Rockafellar, R. T. (Eds.) (2006). *Nonsmooth Mechanics and Analysis. Theoretical and Numerical Advances*. Springer New York, NY. https://doi.org/10.1007/0-387-29195-4.

ASTM International (2013). *ASTM International Technical Committee F42 on Additive Manufacturing Technologies*. 19428.

Bayat, M., Klingaa, C. G., Mohanty, S., De Baere, D., Thorborg, J., Tiedje, N. S., & Hattel, J. H. (2020). Part-scale thermo-mechanical modelling of distortions in laser powder bed fusion – analysis of the sequential flash heating method with experimental validation. *Additive Manufacturing*, *36*, 101508. https://doi.org/10.1016/j.addma.2020.101508.

Chua, C., Liu, Y., Williams, R. J., Chua, C. K., & Sing, S. L. (2024). In-process and post-process strategies for part quality assessment in metal powder bed fusion: A review. *Journal of Manufacturing Systems*, *73*, 75–105. https://doi.org/10.1016/j.jmsy.2024.01.004.

Crespo, A., & Vilar, R. (2010). Finite element analysis of the rapid manufacturing of Ti-6Al-4V parts by laser powder deposition. *Scripta Materialia*, *63*(1), 140–143. https://doi.org/10.1016/j.scriptamat.2010.03.036.

Darabi, R., Ferreira, A., Azinpour, E., Cesar de Sa, J., & Reis, A. (2022). Thermal study of a cladding layer of Inconel 625 in Directed Energy Deposition (DED) process using a phase-field model. *The International Journal of Advanced Manufacturing Technology*, *119*(5), 3975–3993. https://doi.org/10.1007/s00170-021-08376-6.

Darabi, R., Azinpour, E., Reis, A., & Cesar de Sa, J. (2023). Multi-scale multi-physics phase-field coupled thermo-mechanical approach for modeling of powder bed fusion process. *Applied Mathematical Modelling*, *122*, 572–597. https://doi.org/10.1016/j.apm.2023.06.021.

Duxbury, P. M. (2011). *Statistical Physics (PHY831): Part 4: Ginzburg-Landau theory, modeling of dynamics and scaling in complex systems* [Lecture notes]. https://web.pa.msu.edu/people/duxbury/courses/phy831/LectureNotesAndProblems-Part4.pdf.

Gonzalez-Ferreiro, B., Gomez, H., & Romero, I. (2014). A thermodynamically consistent numerical method for a phase field model of solidification. *Communications in Nonlinear Science and Numerical Simulation*, *19*(7), 2309–2323. https://doi.org/10.1016/j.cnsns.2013.11.016.

Heigel, J. C., Michaleris, P., & Reutzel, E. W. (2015). Thermo-mechanical model development and validation of directed energy deposition additive manufacturing of Ti-6Al-4V. *Additive Manufacturing*, *5*, 9–19. https://doi.org/10.1016/j.addma.2014.10.003.

Hodge, N. E., Ferencz, R. M., & Solberg, J. M. (2014). Implementation of a thermomechanical model for the simulation of selective laser melting. *Computational Mechanics*, *54*(1), 33–51. https://doi.org/10.1007/s00466-014-1024-2.

Horn, M., Schmitt, M., Langer, L., Schlick, G., & Seidel, C. (2024). Laser powder bed fusion recoater selection guide – comparison of resulting powder bed properties and part quality. *Powder Technology*, *434*, 119356. https://doi.org/10.1016/j.powtec.2023.119356.

Hughes, T. J. R. (1987). *The Finite Element Method: Linear Static and Dynamic Finite Element Analysis*. Prentice-Hall.

Kollmannsberger, S., Carraturo, M., Reali, A., & Auricchio, F. (2019). Accurate prediction of melt pool shapes in laser powder bed fusion by the non-linear temperature equation including phase changes. *Integrating Materials and Manufacturing Innovation*, *8*(2), 167–177. https://doi.org/10.1007/s40192-019-00132-9.

Labudovic, M., Hu, D., & Kovacevic, R. (2003). A three dimensional model for direct laser metal powder deposition and rapid prototyping. *Journal of Materials Science*, *38*(1), 35–49. https://doi.org/10.1023/A:1021153513925.

Marcus, H. L., Beaman, J. J., Barlow, J. W., Bourell, D. L., & Crawford, R. H. (Eds.) (1992). *Solid Freeform Fabrication Proceedings. September 1992*. The University of Texas at Austin.

Muránsky, O., Hamelin, C. J., Patel, V. I., Luzin, V., & Braham, C. (2015). The influence of constitutive material models on accumulated plastic strain in finite element weld analyses. *International Journal of Solids and Structures*, *69–70*, 518–530. https://doi.org/10.1016/j.ijsolstr.2015.04.032.

Noll, I., Bartel, T., & Menzel, A. (2020). A computational phase transformation model for selective laser melting processes. *Computational Mechanics*, *66*(6), 1321–1342. https://doi.org/10.1007/s00466-020-01903-4.

Novick-Cohen, A. (2008). *Chapter 4. The Cahn–Hilliard equation*. In C. M. Dafermos & M. Pokorný (Eds.), *Handbook of Differential Equations: Evolutionary Equations* (Vol. 4, pp. 201–228). Elsevier. https://doi.org/10.1016/S1874-5717(08)00004-2.

Peng, H., Ghasri-Khouzani, M., Gong, S., Attardo, R., Ostiguy, P., Rogge, R. B., Gatrell, B. A., Budzinski, J., Tomonto, C., Neidig, J., Shankar, M. R., Billo, R., Go, D. B., & Hoelzle, D. (2018). Fast prediction of thermal distortion in metal powder bed fusion additive manufacturing: Part 2, a quasi-static thermo-mechanical model. *Additive Manufacturing*, *22*, 869–882. https://doi.org/10.1016/j.addma.2018.05.001.

Penrose, O., & Fife, P. C. (1990). Thermodynamically consistent models of phase-field type for the kinetic of phase transitions. *Physica D: Nonlinear Phenomena*, *43*(1), 44–62. https://doi.org/10.1016/0167-2789(90)90015-H.

Roy, S., Juha, M., Shephard, M. S., & Maniatty, A. M. (2018). Heat transfer model and finite element formulation for simulation of selective laser melting. *Computational Mechanics*, *62*(3), 273–284. https://doi.org/10.1007/s00466-017-1496-y.

Stender, M. E., Beghini, L. L., Sugar, J. D., Veilleux, M. G., Subia, S. R., Smith, T. R., San Marchi, Ch. W., Brown, A. A., & Dagel, D. J. (2018). A thermal-mechanical finite element workflow for directed energy deposition additive manufacturing process modeling. *Additive Manufacturing*, *21*, 556–566. https://doi.org/10.1016/j.addma.2018.04.012.

Szost, B. A., Terzi, S., Martina, F., Boisselier, D., Prytuliak, A., Pirling, T., Hofmann, M., & Jarvis, D. J. (2016). A comparative study of additive manufacturing techniques: Residual stress and microstructural analysis of CLAD and WAAM printed ti–6Al–4V components. *Materials & Design*, *89*, 559–567. https://doi.org/10.1016/j.matdes.2015.09.115.

Tan, H., Fang, Y., Zhong, C., Yuan, Z., Fan, W., Li, Z., Chen, J., & Lin, X. (2020). Investigation of heating behavior of laser beam on powder stream in directed energy deposition. *Surface and Coatings Technology*, *397*, 126061. https://doi.org/10.1016/j.surfcoat.2020.126061.

Thompson, S. M., Bian, L., Shamsaei, N., & Yadollahi, A. (2015). An overview of Direct Laser Deposition for additive manufacturing; Part I: Transport phenomena, modeling and diagnostics. *Additive Manufacturing*, *8*, 36–62. https://doi.org/10.1016/j.addma.2015.07.001.

Tian, J., Xu, P., & Liu, Q. (2020). Effects of stress-induced solid phase transformations on residual stress in laser cladding a Fe-Mn-Si-Cr-Ni alloy coating. *Materials and Design*, *193*, 108824. https://doi.org/10.1016/j.matdes.2020.108824.

Wang, J.-h., Han, F.-z., Chen, S.-f., & Ying, W.-s. (2019). A novel model of laser energy attenuation by powder particles for laser solid forming. *International Journal of Machine Tools and Manufacture*, *145*, 103440. https://doi.org/10.1016/j.ijmachtools.2019.103440.

Wang, Q., Li, J., Gouge, M., Nassar, A. R., Michaleris, P., & Reutzel, E. W. (2017). Physics-based multivariable modeling and feedback linearization control of melt-pool geometry and temperature in directed energy deposition. *Journal of Manufacturing Science and Engineering*, *Transactions of the ASME*, *139*(2), 1–12. https://doi.org/10.1115/1.4034304.

Wang, S.-L., Sekerka, R. F., Wheeler, A. A., Murray, B. T., Coriell, S. R., Braun, R. J., & McFadden, G. B. (1993). Thermodynamically-consistent phase-field models for solidification. *Physica D: Nonlinear Phenomena*, *69*(1), 189–200. https://doi.org/10.1016/0167-2789(93)90189-8.

Warner, J. H., Ringer, S. P., & Proust, G. (2024). Strategies for metallic powder reuse in powder bed fusion: A review. *Journal of Manufacturing Processes*, *110*, 263–290. https://doi.org/10.1016/j.jmapro.2023.12.066.

Williams, R. J., Davies, C. M., & Hooper, P. A. (2018). A pragmatic part scale model for residual stress and distortion prediction in powder bed fusion. *Additive Manufacturing*, *22*, 416–425. https://doi.org/10.1016/j.addma.2018.05.038.

Zhang, Y., Chen, Q., Guillemot, G., Gandin, C. A., & Bellet, M. (2018). Numerical modelling of fluid and solid thermomechanics in additive manufacturing by powder-bed fusion: Continuum and level set formulation applied to track- and part-scale simulations. *Comptes Rendus – Mécanique*, *346*(11), 1055–1071. https://doi.org/10.1016/j.crme.2018.08.008.

Zhou, Y., Jiang, D., Al-Akailah, A., & Ning, F. (2024). Understanding the formation of laser-induced melt pools with both wire and powder feeding in directed energy deposition. *Additive Manufacturing*, *89*, 104312. https://doi.org/10.1016/j.addma.2024.104312.

Zienkiewicz, O. C., Taylor, R. L., & Zhu, J. Z. (2013). *The finite element method: Its basis and fundamentals* (7th ed.). Butterworth-Heinemann. https://doi.org/10.1016/C2009-0-24909-9.